

Boost Converter with Main Switch Possessing ZVT and ZCT and Auxiliary Switch Possessing ZCS

Kuo-Ing Hwu ^{1,*}, Zhi-Fan Lin ² and Pei-Ching Tseng ¹

¹ Department of Electrical Engineering, National Taipei University of Technique, 1, Sec. 3, Zhongxiao E. Rd., Taipei 10608, Taiwan; t111319007@ntut.org.tw

² FSP Technique Inc., No. 22, Jianguo E. Rd., Taoyuan Dist., Taoyuan City 33068, Taiwan; fenlin@fsp-group.com.tw

* Correspondence: eaglehwu@ntut.edu.tw; Tel.: +886-2-27712171 (ext. 2159)

Abstract: In this paper, a zero-voltage and zero-current transition (ZVZCT) boost converter is presented with a small number of auxiliary components, such as a resonant capacitor, a resonant inductor and an auxiliary power switch, to produce a main power switch with both zero-voltage switching (ZVS) and zero-current switching (ZCS). Furthermore, the auxiliary power switch also has zero current switching. In addition, a look-up table is employed to implement an auto-tuning technique to regulate the trigger position and turn-on time of the auxiliary power switch, to further improve efficiency, especially at light load, thereby making the overall efficiency of the converter present a horizontal curve. Moreover, in terms of the system control, the digital controller is implemented directly from the z-domain, and the field programmable gate array (FPGA) is utilized as the system control kernel to achieve a fully digitalized control system. The simulated results are used to demonstrate the feasibility of the proposed converter, whereas the experimental results are used to verify its effectiveness.

Keywords: auto-tuning technique; boost converter; FPGA; fully-digitalized control; z-domain; controller design; ZVZCT; ZVT; ZCT; ZVS; ZCS



Citation: Hwu, K.-I.; Lin, Z.-F.; Tseng, P.-C. Boost Converter with Main Switch Possessing ZVT and ZCT and Auxiliary Switch Possessing ZCS. *Energies* **2023**, *16*, 5504. <https://doi.org/10.3390/en16145504>

Academic Editors: Abdelali El Aroudi and Salvatore Musumeci

Received: 29 May 2023

Revised: 29 June 2023

Accepted: 18 July 2023

Published: 20 July 2023



Copyright: © 2023 by the authors. Licensee MDPI, Basel, Switzerland. This article is an open access article distributed under the terms and conditions of the Creative Commons Attribution (CC BY) license (<https://creativecommons.org/licenses/by/4.0/>).

1. Introduction

As the techniques for using power converters have become more and more developed, high efficiency, high switching frequency, small size and good stability have become the basic requirements. However, as the switching frequency of the converter increases, the switching loss of the power switch also increases, thus reducing the efficiency of the power converter. In order to overcome the impact of traditional hard-switching power converters, the soft switching technique has been developed, which can effectively reduce the switching loss.

The methods of resonant power converters have been presented in [1,2], in which resonant inductors and resonant capacitors are added to converters to form resonant circuits, which are used to change the voltages on power switches or the currents flowing through the power switches to achieve zero-voltage or zero-current switching. However, the disadvantage is that the high voltage or high current caused by the resonance of the auxiliary circuit increases the component stress and, in turn, increases the conduction loss. In addition, since the resonance time of the auxiliary circuit is fixed, it is necessary to add variable frequency control in order to keep the output voltage stable at the prescribed value, which makes the design of the output filter difficult.

The literature [3,4] proposes adding auxiliary power switches and resonant elements to converters to generate resonant circuits to achieve zero-voltage or zero-current switching, and hence the fixed resonant time of the semi-resonant converter when it is on or off is improved, so that the converter does not need variable frequency control, and therefore fixed frequency control can be achieved.

The literature [5,6] also suggests that before the main power switch is turned on, the auxiliary power switch is turned on first or afterwards to form a resonant circuit, and by generating transient resonance, the voltage across the main power switch or the current flowing through the main power switch resonates to zero. This transient resonance occurs only during the instant of power switch switching, and does not resonate during the rest of the time, thus avoiding the problem of high voltage or high current stress, therefore reducing the conduction loss of the converter.

The literature [7,8] has proposed that the auxiliary power switch could generate two transient resonances in each switching cycle without affecting the circuit behavior. The main power switch can achieve zero voltage switching (ZVS) during the first transient resonance and zero current switching (ZCS) during the second transient resonance. Therefore, the main power switch has both ZVS and ZCS, but the disadvantage is that the auxiliary power switch cannot achieve ZVS or ZCS, and it is mostly floating, which not only increases the complexity of the gate driver circuit, but also requires multiple auxiliary components to make the main power switch have both ZVS and ZCS.

The main structure in [9] is an interleaved boost converter, which features only one auxiliary switch with common ground and enables two main switches to realize ZVS and ZCS; the drawback is that the auxiliary switch needs four gate driving signals over one switching cycle, and the resonance condition is strict, which makes the mathematical mode analysis extremely complicated and difficult.

The topology shown in [10] is a two-phase interleaved boost ZVT converter, whose characteristics are different from those shown in [a]. The circuit shown in [b] uses two auxiliary switches to realize the main switch with ZVS turn-on and ZCS turn-off and the used auxiliary switches have ZCS turn-off with only one gate driving signal over one switching cycle, but the drawback is that the two auxiliary switches are floating, thereby making the gate driving more difficult and greatly reducing the practicality of this converter.

The circuit shown in [11] is a simple structure of a boost ZVT converter, which features a zero-current quasi-resonant circuit and an auxiliary switch with MOSFETs in series with diodes combined, and the auxiliary switch possesses common ground. In addition, the advantage is that the current waveform of the main switch has the characteristics of zero-current turn-on and zero-current turn-off, the switching control mode of the converter is fixed frequency, and the structure is simple, easy to analyze and low in cost.

The circuits shown in [12,13] both are boost converters using ZVT and ZCT technologies, but the feature of the circuit shown in [12] is that it is easier to achieve ZVS and ZCS because the main switch and the auxiliary switch are common-grounded, but the drawback is that too many components are used, resulting in higher cost. The circuit shown in [13] uses fewer components for the resonant circuit of the auxiliary switch and is easier to analyze, but the disadvantage is that the condition of the main switch to realize soft switching is more severe and difficult and the soft switching feature cannot be implemented all over the whole load range.

The circuit shown in [14] is a two-phase interleaved four-switch boost ZVT converter, using only one coupling inductor and one clamping capacitor, which is characterized by the ability to give the four main switches ZVS turn-on in the current conduction mode (CCM) without any auxiliary switches. This circuit is characterized by few auxiliary circuit components, easy analysis and ZVS capability for most of the load range. However, the disadvantage is that the auxiliary switch is on the secondary side and floating, which makes the feedback control difficult and the transient response poor.

This circuit shown in [15] is characterized by a small number of components in the auxiliary circuit, easy analysis and the capability for ZVS for most of the load range, but the disadvantage is that the auxiliary switch is on the secondary side and is floating, resulting in a circuit with poor feedback control and poor transient response.

The circuit shown in [16] is a full-bridge DC to AC ZVT converter with an auxiliary circuit using only three components (i.e., one inductor and two MOSFETs) to achieve ZVS turn-on for all four main switches and ZCS turn-off for the auxiliary switch. The

advantage is that a small number of components is used to achieve soft switching, but the disadvantage is that the auxiliary switches are floating.

Reference [17] presents a ZCZVT step-up converter. The advantage of this is that this circuit is the integration of three coupled inductors into a single magnetic element and the auxiliary switch has common ground and a soft switching feature. The disadvantage is that too many components are used to achieve soft switching, thereby making the auxiliary circuit too complex to analyze its operating principle.

Reference [18] proposes a step-up and step-down ZVT converter with a demagnetized auxiliary circuit. The advantage is that the demagnetized winding is used to reduce the voltage stress on the auxiliary circuit, but the disadvantage is that the auxiliary switch is hard-switched.

In this paper, a boost converter with soft switching is developed, which is implemented only by one auxiliary switch, one resonant inductor and one resonant capacitor as compared to the traditional boost converter. In this circuit, the main switch has zero-voltage and zero-current transition (ZVZCT) whereas the auxiliary switch has zero-current switching (ZCS). Aside from this, the PWM auto-tuning technique based on a given lookup table is added to adjust the turn-on instant and turn-on time of the auxiliary switch, so that the efficiency is further upgraded, particularly at light load. Therefore, the curve of efficiency versus load current is made nearly flat all over the load range. Regarding the system control, the digital controller is designed directly from the z-domain.

2. Operating Principle

Figure 1 shows the proposed step-up converter with soft switching, in which the dashed box is the auxiliary circuit, which consists of an auxiliary power switch S_a , a resonant inductor L_r and a resonant capacitor C_r . Figure 2 displays the illustrated waveforms of the proposed converter operating.

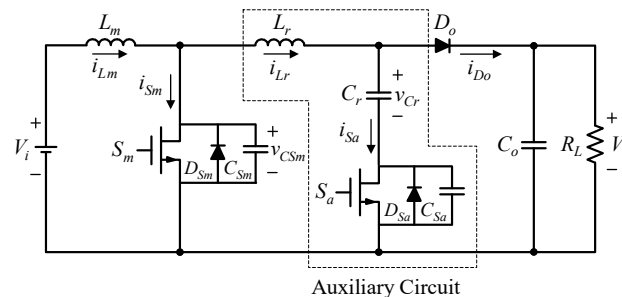


Figure 1. Boost converter with S_a having ZVT and ZVT and S_b having ZCS.

Prior to the analysis, the following assumptions are made:

- (1) The power switches and diodes are regarded as ideal components;
- (2) The parasitic resistances of the inductance and capacitance are negligible;
- (3) The input inductance is extremely large and can be viewed as an ideal constant current source;
- (4) The output capacitance is very large and can be considered as an ideal constant voltage source.

According to the above assumptions, the converter operating can be divided into twelve states over one switching cycle.

State 1 [$t_0 \leq t \leq t_1$]: Before the start of the switching cycle, both the main power switch S_m and the auxiliary power switch S_a are in the off-state, and the output diode D_o is in the on-state. As displayed in Figure 3a at the time t_0 , the auxiliary power switch S_a turns on first, and the auxiliary power switch current i_{S_a} rises rapidly to equal the input current I_{L_m} , causing the output diode D_o to turn off and then state 1 to come to the end.

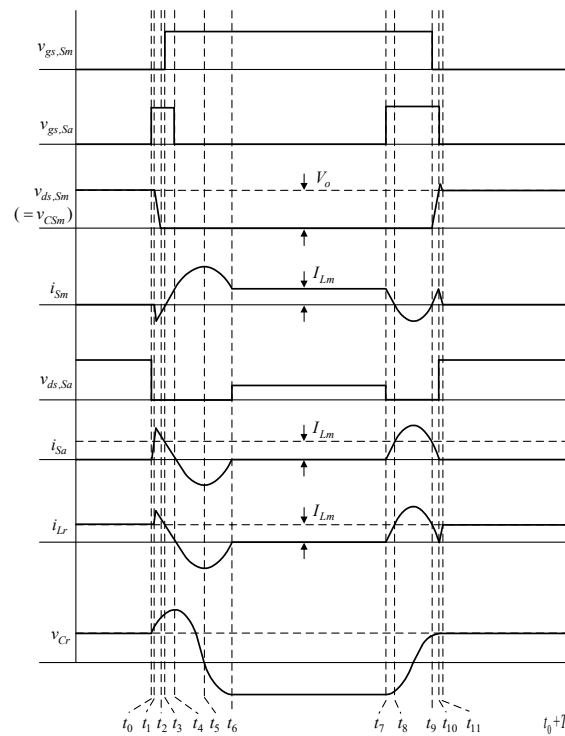


Figure 2. Illustrated waveforms of the proposed converter operating.

The initial current of the resonant inductor is the input current I_{Lm} and the initial voltage of the resonant capacitor is V_{Cr10} .

The corresponding equations in this state are

$$\begin{cases} v_{Cr}(t) = \frac{I_{Lm} - I_o}{C_r}(t - t_0) + V_{Cr10} \\ i_{Lr}(t) = I_{Lm} \end{cases} \quad (1)$$

By substituting the boundary condition $v_{Cr}(t_1) = V_{Cr1}$ into (1), we can find that the corresponding time experienced by this state is

$$T_1 = t_1 - t_0 = \frac{C_r(V_{Cr1} - V_{Cr10})}{(I_{Lm} - I_o)} \quad (2)$$

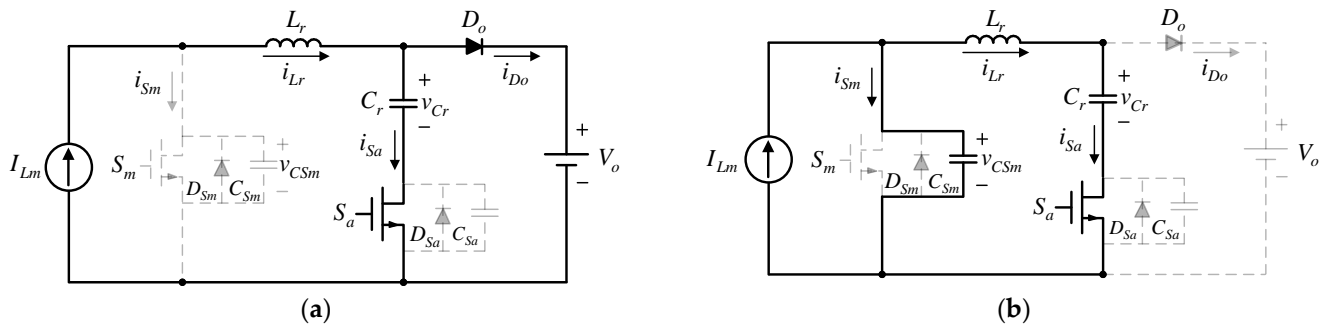


Figure 3. Cont.

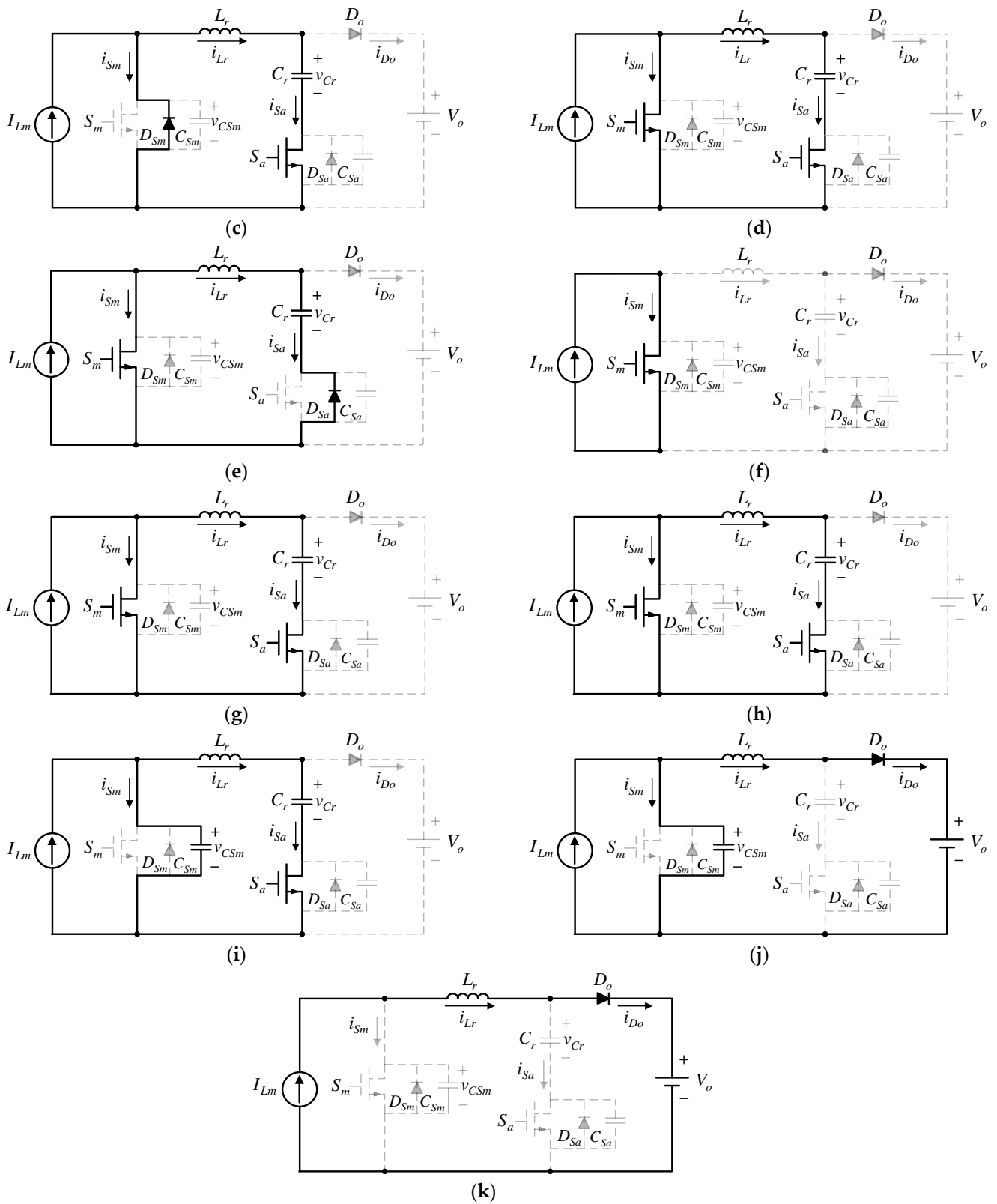


Figure 3. (a). Current path: state 1. (b). Current path: state 2. (c). Current path: state 3. (d). Current path: state 4. (e). Current path: state 5 and 6. (f). Current path: state 7. (g). Current path: state 8. (h). Current path: state 9. (i). Current path: state 10. (j). Current path: state 11. (k). Current path: state 12.

State 2 [$t_1 \leq t \leq t_2$]: As displayed in Figure 3b, when the auxiliary power switch current i_{Sa} rises to the input current I_{Lm} , the parasitic capacitor C_{Sm} of the main power switch discharges. When the parasitic capacitor C_{Sm} of the main power switch discharges to zero, state 2 ends.

The initial current of the resonant inductor is the input current I_{Lm} , the initial voltage of the resonant capacitor is V_{Cr1} , and the initial voltage of the parasitic capacitor across the main power switch is V_o .

The corresponding equations in this state are

$$\begin{cases} i_{Lr}(t) = \frac{(V_o - V_{Cr1})}{Z_1} \sin \omega_1(t - t_1) + \frac{C}{C_r} I_{Lm} \cos \omega_1(t - t_1) + \frac{C}{C_{Sm}} I_{Lm} \\ v_{Cr}(t) = \frac{C}{C_r} \left[\frac{I_{Lm}}{C_r \omega_1} \sin \omega_1(t - t_1) - (V_o - V_{Cr1}) \cos \omega_1(t - t_1) + (V_o - V_{Cr1}) \right] + \frac{I_{Lm}}{C_r + C_{Sm}} (t - t_1) + V_{Cr1} \\ v_{CSm}(t) = -\frac{C}{C_{Sm}} \left[\frac{I_{Lm}}{C_r \omega_1} \sin \omega_1(t - t_1) - (V_o - V_{Cr1}) \cos \omega_1(t - t_1) + (V_o - V_{Cr1}) \right] + \frac{I_{Lm}}{C_r + C_{Sm}} (t - t_1) + V_o \end{cases} \quad (3)$$

where

$$\omega_1 = \frac{1}{\sqrt{L_r C}}, \quad Z_1 = \sqrt{\frac{L_r}{C}}, \quad C = \frac{C_r C_{Sm}}{C_r + C_{Sm}} \quad (4)$$

By substituting the boundary conditions into (3), we can find the corresponding time taken by this state is

$$T_2 = t_2 - t_1 = \frac{1}{\omega_1} \left[\frac{Z_1 (I_{Lr2} - I_{Lm})}{V_o - V_{Cr1}} \right] \quad (5)$$

State 3 [$t_2 \leq t \leq t_3$]: As displayed in Figure 3c, when the parasitic capacitance C_{Sm} of the main power switch is discharged to zero, the body diode D_{Sm} of the main power switch S_m is turned on. The initial current of resonant inductor is I_{Lr2} and the initial voltage of the resonant capacitor is V_{Cr2} .

The corresponding equations in this state are

$$\begin{cases} i_{Lr}(t) = I_{Lr2} \cos \omega_2(t - t_2) - \frac{V_{Cr2}}{Z_2} \sin \omega_2(t - t_2) \\ v_{Cr}(t) = V_{Cr2} \cos \omega_2(t - t_2) + Z_2 I_{Lr2} \sin \omega_2(t - t_2) \end{cases} \quad (6)$$

where

$$\omega_2 = \frac{1}{\sqrt{L_r C_r}}, \quad Z_2 = \sqrt{\frac{L_r}{C_r}} \quad (7)$$

By substituting the boundary conditions into (6), we can find the corresponding time experienced by this state is

$$T_3 = t_3 - t_2 = \frac{1}{\omega_2} \left[\frac{Z_2 (I_{Lr2} - I_{Lm})}{V_{Cr2}} \right] \quad (8)$$

State 4 [$t_3 \leq t \leq t_4$]: As shown in Figure 3d, when the main power switch S_m is turned on with ZVS, the main power switch current i_{Sm} starts to rise from zero to the input current I_{Lm} . At this time, the auxiliary power switch S_a is turned off with ZCS.

The initial current of the resonant inductor is I_{Lm} , and the initial voltage of the resonant capacitor is V_{Cr3} .

The corresponding equations in this state are

$$\begin{cases} i_{Lr}(t) = I_{Lm} \cos \omega_2(t - t_3) - \frac{V_{Cr3}}{Z_2} \sin \omega_2(t - t_3) \\ v_{Cr}(t) = V_{Cr3} \cos \omega_2(t - t_3) + Z_2 I_{Lm} \sin \omega_2(t - t_3) \end{cases} \quad (9)$$

By substituting the boundary conditions into (9), we can find the time experienced by this state is

$$T_4 = t_4 - t_3 = \frac{1}{\omega_2} \left[\frac{Z_2 I_{Lm}}{V_{Cr3}} \right] \quad (10)$$

State 5 [$t_4 \leq t \leq t_5$]: As displayed in Figure 3e, when the main power switching current i_{Sm} is greater than the input current I_{Lm} , the resonant inductor current i_{Lr} starts to flow in the opposite direction. When the resonant capacitor C_r is discharged to zero, state 5 ends.

The initial current of the resonant inductor is zero, and the initial voltage of the resonant capacitor is V_{Cr4} .

The corresponding equations in this state are

$$\begin{cases} i_{Lr}(t) = -\frac{V_{Cr4}}{Z_2} \sin \omega_2(t - t_4) \\ v_{Cr}(t) = V_{Cr4} \cos \omega_2(t - t_4) \end{cases} \quad (11)$$

By substituting the boundary conditions into (11), we can find the time taken by this state is

$$T_5 = t_5 - t_4 = \frac{1}{\omega_2} \left[\frac{Z_2 I_{Lr5}}{V_{Cr4}} \right] \quad (12)$$

State 6 [$t_5 \leq t \leq t_6$]: As displayed in Figure 3e, this state continues to resonate. When the resonant inductor current i_{Lr} resonates to zero, this state comes to end.

The initial current of the resonant inductor is I_{Lr5} , and the initial voltage of the resonant capacitor is zero.

The corresponding equations in this state are

$$\begin{cases} i_{Lr}(t) = -I_{Lr5} \cos \omega_2(t - t_5) \\ v_{Cr}(t) = -Z_2 I_{Lr5} \sin \omega_2(t - t_5) \end{cases} \quad (13)$$

By substituting the boundary conditions into (13), we can find the time experienced by this state is

$$T_6 = t_6 - t_5 = \frac{1}{\omega_2} \left[\frac{V_{Cr6}}{Z_2 I_{Lr5}} \right] \quad (14)$$

State 7 [$t_6 \leq t \leq t_7$]: As displayed in Figure 3f, this state is like the magnetization state of the traditional boost converter, where the output capacitor C_o provides energy to the load. When the auxiliary power switch S_a is turned on again, this state ends.

State 8 [$t_7 \leq t \leq t_8$]: As displayed in Figure 3g, when the auxiliary power switch S_a is turned on, the resonant inductor current i_{Lr} rises to the input current I_{Lm} , and then state 8 comes to an end.

The initial current of the resonant inductor is zero, and the initial voltage of the resonant capacitor is $-V_{Cr7}$.

The corresponding equations in this state are

$$\begin{cases} i_{Lr}(t) = \frac{V_{Cr7}}{Z_2} \sin \omega_2(t - t_7) \\ v_{Cr}(t) = -V_{Cr7} \cos \omega_2(t - t_7) \end{cases} \quad (15)$$

By substituting the boundary conditions into (15), we can find the time experienced by this state is

$$T_8 = t_8 - t_7 = \frac{1}{\omega_2} \left[\frac{Z_2 I_{Lm}}{V_{Cr7}} \right] \quad (16)$$

State 9 [$t_8 \leq t \leq t_9$]: As shown in Figure 3h, when the resonant inductor current i_{Lr} is greater than the input current I_{Lm} , the main power switch current i_{Sm} starts to flow in the opposite direction. When the inductor current resonates to the input current I_{Lm} again, the main power switch is turned off at this time, so that the main power switch has ZCS turn-on.

The initial current of the resonant inductor is I_{Lm} , and the initial voltage of the resonant capacitor is $-V_{Cr8}$.

The corresponding equations in this state is

$$\begin{cases} i_{Lr}(t) = I_{Lm} \cos \omega_2(t - t_8) + \frac{V_{Cr8}}{Z_2} \sin \omega_2(t - t_8) \\ v_{Cr}(t) = -V_{Cr8} \cos \omega_2(t - t_8) + Z_2 I_{Lm} \sin \omega_2(t - t_8) \end{cases} \quad (17)$$

By substituting the boundary conditions into (17), we can find the time taken by this state is

$$T_9 = t_9 - t_8 = \frac{1}{\omega_2} \left[\frac{V_{Cr9} + V_{Cr8}}{Z_2 I_{Lm}} \right] \quad (18)$$

State 10 [$t_9 \leq t \leq t_{10}$]: As shown in Figure 3i, when the resonant inductor current i_{Lr} drops to zero, the auxiliary power switch S_a is turned off with ZCS. Once the auxiliary power switch is turned off, this state ends.

The initial current of the resonant inductor is I_{Lm} , the initial voltage of the resonant capacitor is V_{Cr9} , and the initial voltage of the parasitic capacitor of the main power switch is zero.

The corresponding equations of this state is

$$\begin{cases} i_{Lr}(t) = \frac{-V_{Cr9}}{Z_1} \sin \omega_1(t - t_9) + \frac{C}{C_r} I_{Lm} \cos \omega_1(t - t_9) + \frac{C}{C_{Sm}} I_{Lm} \\ v_{Cr}(t) = \frac{C}{C_r} \left[\frac{I_{Lm}}{C_r \omega_1} \sin \omega_1(t - t_9) + V_{Cr9} \cos \omega_1(t - t_9) - V_{Cr9} \right] + \frac{I_{Lm}}{C_r + C_{Sm}} (t - t_9) + V_{Cr9} \\ v_{CSm}(t) = -\frac{C}{C_{Sm}} \left[\frac{I_{Lm}}{C_r \omega_1} \sin \omega_1(t - t_9) + V_{Cr9} \cos \omega_1(t - t_9) - V_{Cr9} \right] + \frac{I_{Lm}}{C_r + C_{Sm}} (t - t_9) \end{cases} \quad (19)$$

By substituting the boundary conditions into (19), we can find the time experienced by this state is

$$T_{10} = t_{10} - t_9 = \frac{1}{\omega_1} \left[\frac{Z_1 I_{Lm}}{V_{Cr9}} \right] \quad (20)$$

State 11 [$t_{10} \leq t \leq t_{11}$]: As shown in Figure 3j, when the voltage v_{CSm} on the parasitic capacitance of the main power switch rises above the output voltage V_o and the resonant inductor current rises linearly from zero to the input current I_{Lm} , this state 11 ends.

The initial current of the resonant inductor is zero, and the initial voltage of the parasitic capacitor of the main power switch is V_{CSm10} .

The corresponding equations of state in this state are

$$\begin{cases} i_{Lr}(t) = I_{Lm} - I_{Lm} \cos \omega_{10}(t - t_{10}) + \frac{(V_{CSm10} - V_o)}{Z_{10}} \sin \omega_{10}(t - t_{10}) \\ v_{CSm}(t) = V_o + (V_{CSm10} - V_o) \cos \omega_{10}(t - t_{10}) + Z_{10} I_{Lm} \sin \omega_{10}(t - t_{10}) \end{cases} \quad (21)$$

where

$$\omega_{10} = \frac{1}{\sqrt{L_r C_{Sm}}}, Z_{10} = \sqrt{\frac{L_r}{C_{Sm}}} \quad (22)$$

By substituting the boundary conditions into (21), we can find the time experienced in this state is

$$T_{11} = t_{11} - t_{10} = \frac{1}{\omega_{10}} \left[\frac{Z_{10} I_{Lm}}{V_{CSm10} - V_o} \right] \quad (23)$$

State 12 [$t_{11} \leq t \leq t_0 + T_s$]: As shown in Figure 3k, this state is just like the input inductor demagnetization state of the traditional boost converter, sending energy to the output. When the auxiliary power switch S_a is turned on again, this state ends and returns to state 1.

After deducing from the above-mentioned states, the soft switching status of the power switch can be found from Table 1.

Table 1. Soft switching status of the power switches.

State	Power Switch	Soft Switching Status
3	S_m	ZVT turn-on
4	S_a	ZCS turn-off
9	S_m	ZCT turn-off
10	S_a	ZCS turn-off

Table 1 display soft switching status of the power switches.

3. Modeling Based on Dual Time Scale Averaging Method

In this paper, the averaging method for dual time scale [19] is used to derive the small-signal mathematical model of the proposed circuit. This averaging method can be used to classify the system into slow state variables and fast state variables. The slow state variables are input inductance current i_{Lm} and output capacitance voltage v_{Co} , and the fast state variables are resonant capacitance voltage v_{Cr} and resonant inductor current i_{Lr} . Figure 4 shows the equivalent circuit of the converter used after averaging. The dashed line shows the averaging mode of the fast state variables relative to the slow state variables.

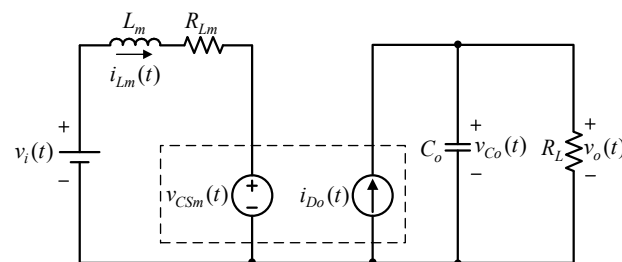


Figure 4. Equivalent circuit after averaging.

The equations for the slow state variables can be listed from Figure 4 as

$$\begin{cases} \frac{di_{Lm}(t)}{dt} = \frac{v_i(t)}{L_m} - \frac{R_{Lm}}{L_m} i_{Lm}(t) - \frac{v_{CSm}(t)}{L_m} \\ \frac{dv_{Co}(t)}{dt} = -\frac{v_{Co}(t)}{C_o R_L} + \frac{i_{Do}(t)}{C_o} \end{cases} \quad (24)$$

$$v_o(t) = v_{Co}(t) \quad (25)$$

where $v_{CSm}(t)$ is the average function of the main power switch over one switching period T_s , i.e., $v_{CSm}(t) = \langle v_{CSm}(t) \rangle_{T_s}$; $i_{Do}(t)$ is the average function of the output diode current over one switching period T_s , i.e., $i_{Do}(t) = \langle i_{Do}(t) \rangle_{T_s}$. Therefore, the averaging mode of the slow state variables can be obtained by finding the average function of $v_{CSm}(t)$ and $i_{Do}(t)$. The symbols are defined herein first to reduce the complexity of the analysis, as follows:

$$\begin{cases} i_{Lm}(t) = i_{Lm} \\ v_o(t) = v_o \\ v_{Co}(t) = v_{Co} \\ v_i(t) = v_i \\ d(t) = d \\ d'(t) = d' = 1 - d \\ v_{CSm}(t) = v_{CSm} \\ i_{Do}(t) = i_{Do} \end{cases} \quad (26)$$

where each time function includes the DC component and the AC small-signal component.

The definition of the average function of v_{CSm} , i.e., $\langle v_{CSm} \rangle_{T_s} = \langle v_{CSm}(t) \rangle_{T_s} = \frac{1}{T_s} \sum_{i=0}^{11} \int_{t_i}^{t_{i+1}} v_{CSm}(\tau) d\tau$ and the average function of i_{D0} , i.e., $\langle i_{D0} \rangle_{T_s} = \langle i_{D0}(t) \rangle_{T_s} = \frac{1}{T_s} \sum_{i=0}^{11} \int_{t_i}^{t_{i+1}} i_{D0}(\tau) d\tau$ and the solution v_{CSm} and i_{D0} at each state can be obtained from the derivation in Section 2, as follows:

$$\begin{aligned} \langle v_{CSm} \rangle_{T_s} &= \frac{1}{T_s} \sum_{i=0}^{11} \int_{t_i}^{t_{i+1}} v_{CSm}(\tau) d\tau \\ &= \frac{1}{T_s} \left\{ v_o T_1 + \left[\frac{C}{C_{Sm}} \frac{1}{\omega_1} (v_o - V_{Cr1}) \sin \omega_1 T_2 - \frac{C}{C_{Sm}} (v_o - V_{Cr1}) T_2 + V_{Cr1} T_2 \right] \right. \\ &\quad + \left[-\frac{C}{C_{Sm}} \frac{1}{\omega_1} V_{Cr9} \sin \omega_1 T_{10} + \frac{C}{C_{Sm}} V_{Cr9} T_{10} \right] \\ &\quad + \left[v_o T_{11} + \frac{1}{\omega_{10}} (V_{CSm10} - v_o) \sin \omega_{10} T_{11} + \frac{1}{2} Z_{10} i_{Lm} \omega_{10} T_{11}^2 \right] \\ &\quad \left. + v_o [d' T_s - (T_{10} + T_{11})] \right\} \end{aligned} \tag{27}$$

$$\begin{aligned} \langle i_{D0} \rangle_{T_s} &= \frac{1}{T_s} \sum_{i=0}^{11} \int_{t_i}^{t_{i+1}} i_{D0}(\tau) d\tau \\ &= \frac{1}{T_s} \left[\int_{t_0}^{t_1} \frac{v_o}{R_L} d\tau + \int_{t_{10}}^{t_{11}} \frac{v_o}{R_L} d\tau + \int_{t_{11}}^{t_0} i_{Lm} d\tau \right] \\ &= \frac{1}{T_s} \left\{ \frac{v_o}{R_L} T_1 + \frac{v_o}{R_L} T_{11} + i_{Lm} [d' T_s - (T_{10} + T_{11})] \right\} \end{aligned} \tag{28}$$

Equations (27) and (28) can be expressed as

$$\begin{cases} \langle v_{CSm} \rangle_{T_s} = f_{vCSm}(v_o, i_{Lm}, d') = v_o d' + f_{vCSm}(v_o, i_{Lm}) \\ \langle i_{D0} \rangle_{T_s} = f_{iD0}(v_o, i_{Lm}, d') = i_{Lm} d' + f_{iD0}(v_o, i_{Lm}) \end{cases} \tag{29}$$

where

$$\begin{cases} \langle v_{CSm} \rangle_{T_s} = V_{CSm} + \tilde{v}_{CSm}, |\tilde{v}_{CSm}| \ll V_{CSm} \\ \langle i_{D0} \rangle_{T_s} = I_{D0} + \tilde{i}_{D0}, |\tilde{i}_{D0}| \ll I_{D0} \end{cases} \tag{30}$$

Equations (24) and (25) can be rewritten according to Equation (30) as

$$\begin{bmatrix} \frac{di_{Lm}}{dt} \\ \frac{dv_{Co}}{dt} \end{bmatrix} = \begin{bmatrix} -\frac{R_{Lm}}{L_m} & 0 \\ 0 & -\frac{1}{C_o R_L} \end{bmatrix} \begin{bmatrix} i_{Lm} \\ v_{Co} \end{bmatrix} + \begin{bmatrix} \frac{1}{L_m} \\ 0 \end{bmatrix} v_i + \begin{bmatrix} -\frac{1}{L_m} & 0 \\ 0 & \frac{1}{C_o} \end{bmatrix} \begin{bmatrix} V_{CSm} + \tilde{v}_{CSm} \\ I_{D0} + \tilde{i}_{D0} \end{bmatrix} \tag{31}$$

$$v_o(t) = \begin{bmatrix} 0 & 1 \end{bmatrix} \begin{bmatrix} i_{Lm} \\ v_{Co} \end{bmatrix} \tag{32}$$

Since there are nonlinear terms in (29), differential equations based on the averaging mode are nonlinear. To obtain linear equations, Taylor series expansions at the DC operating point of the converter must be performed to remove nonlinear terms, and so that

$$\begin{cases} \langle v_{CSm} \rangle_{T_s} = (V_o + \tilde{v}_o)(D' - \tilde{d}) + \frac{\partial f_{vCSm}(v_o, i_{Lm})}{\partial v_o} \tilde{v}_o + \frac{\partial f_{vCSm}(v_o, i_{Lm})}{\partial i_{Lm}} \tilde{i}_{Lm} \\ \langle i_{D0} \rangle_{T_s} = (I_{Lm} + \tilde{i}_{Lm})(D' - \tilde{d}) + \frac{\partial f_{iD0}(v_o, i_{Lm})}{\partial v_o} \tilde{v}_o + \frac{\partial f_{iD0}(v_o, i_{Lm})}{\partial i_{Lm}} \tilde{i}_{Lm} \end{cases} \tag{33}$$

where the small-signal AC equations are

$$\begin{cases} \tilde{v}_{CSm} = \left[D' + \frac{\partial f_{vCSm}(v_o, i_{Lm})}{\partial v_o} \right] \tilde{v}_o + \frac{\partial f_{vCSm}(v_o, i_{Lm})}{\partial i_{Lm}} \tilde{i}_{Lm} - V_o \tilde{d} \\ \tilde{i}_{D0} = \frac{\partial f_{iD0}(v_o, i_{Lm})}{\partial v_o} \tilde{v}_o + \left[D' + \frac{\partial f_{iD0}(v_o, i_{Lm})}{\partial i_{Lm}} \right] \tilde{i}_{Lm} - I_{Lm} \tilde{d} \end{cases} \tag{34}$$

At the quiescent DC operating point, applying (34) and small-signal AC disturbances shown in (35) to (31) and (32) can obtain (36) and (37), as follows:

$$\begin{cases} v_i = V_i + \tilde{v}_i \\ v_o = V_o + \tilde{v}_o \\ i_{Lm} = I_{Lm} + \tilde{i}_{Lm} \\ d = D + \tilde{d} \\ d' = D' - \tilde{d}' \end{cases} \quad (35)$$

$$\begin{bmatrix} \frac{d\tilde{i}_{Lm}}{dt} \\ \frac{d\tilde{v}_o}{dt} \end{bmatrix} = \begin{bmatrix} -\frac{R_{Lm}}{L_m} & \frac{-D'}{L_m} \\ \frac{D'}{R_L C_o} & \frac{-1}{R_L C_o} \end{bmatrix} \begin{bmatrix} \tilde{i}_{Lm} \\ \tilde{v}_o \end{bmatrix} + \begin{bmatrix} \frac{1}{L_m} & \frac{V_o}{L_m} \\ 0 & \frac{-I_{Lm}}{C_o} \end{bmatrix} \begin{bmatrix} \tilde{v}_i \\ \tilde{d} \end{bmatrix} + \begin{bmatrix} \frac{-\partial f_{vCSm}(v_o, i_{Lm})}{\partial i_{Lm}} & \frac{-\partial f_{vCSm}(v_o, i_{Lm})}{\partial v_o} \\ \frac{\partial f_{iD_o}(v_o, i_{Lm})}{\partial i_{Lm}} & \frac{\partial f_{iD_o}(v_o, i_{Lm})}{\partial v_o} \end{bmatrix} \begin{bmatrix} \tilde{i}_{Lm} \\ \tilde{v}_o \end{bmatrix} \quad (36)$$

$$\tilde{v}_o = [0 \quad 1] \begin{bmatrix} \tilde{i}_{Lm} \\ \tilde{v}_{C_o} \end{bmatrix} \quad (37)$$

After obtaining (36), the transfer function $G_{vg}(s)$ of input voltage \tilde{v}_i to output voltage \tilde{v}_o and the transfer function $G_{vd}(s)$ of duty cycle \tilde{d} to output voltage \tilde{v}_o can be obtained as follows:

$$G_{vg}(s) = \frac{D'}{L_m C_o} + \frac{\frac{\partial f_{iD_o}(v_o, i_{Lm})}{\partial i_{Lm}}}{\frac{\partial f_{vCSm}(v_o, i_{Lm})}{\partial i_{Lm}}} \quad (38)$$

$$G_{vd}(s) = \frac{-\frac{I_{Lm}}{C_o} s + \frac{1}{L_m C_o} (-R_{Lm} I_{Lm} + D' V_o)}{\text{den}(s)} + \frac{1}{L_m C_o} \left[\frac{-\frac{\partial f_{vCSm}(v_o, i_{Lm})}{\partial i_{Lm}} I_{Lm} + \frac{\partial f_{iD_o}(v_o, i_{Lm})}{\partial i_{Lm}} V_o}{\text{den}(s)} \right] \quad (39)$$

where the denominator is defined as

$$\begin{aligned} \text{den}(s) = & s^2 + \left(\frac{1}{R_L C_o} + \frac{R_{Lm}}{L_m} \right) s + \frac{1}{R_L L_m C_o} (R_{Lm} + D'^2 R_L) + \left[\frac{\frac{\partial f_{vCSm}(v_o, i_{Lm})}{\partial i_{Lm}}}{L_m} - \frac{\frac{\partial f_{iD_o}(v_o, i_{Lm})}{\partial v_o}}{C_o} \right] s \\ & + \frac{1}{R_L L_m C_o} \left[\frac{\partial f_{vCSm}(v_o, i_{Lm})}{\partial i_{Lm}} - (R_{Lm} + \frac{\partial f_{vCSm}(v_o, i_{Lm})}{\partial i_{Lm}}) \frac{\partial f_{iD_o}(v_o, i_{Lm})}{\partial v_o} \right] R_L \\ & + R_L D' \left(\frac{\partial f_{vCSm}(v_o, i_{Lm})}{\partial v_o} + \frac{\partial f_{iD_o}(v_o, i_{Lm})}{\partial i_{Lm}} \right) + R_L \frac{\partial f_{vCSm}(v_o, i_{Lm})}{\partial v_o} \frac{\partial f_{iD_o}(v_o, i_{Lm})}{\partial i_{Lm}} \end{aligned} \quad (40)$$

Table 2 shows the system and component specifications.

Table 2. System and component specifications.

Name	Specification
System Operation Mode	Continuous Conduction Mode (CCM)
Rated Input Voltage V_i	156 V
Rated Output Voltage V_o	200 V
System Switching Frequency f_s /Period T_s	100 kHz/10 μ s
Rated Output Current $I_{o, rated}$ /Power $P_{o, rated}$	2 A/400 W
Minimum Output Current $I_{o, min}$ /Power $P_{o, min}$	0.2 A/40 W
Input Inductance L_m /Output Capacitance C_o	1 m H/470 μ F
Resonance Inductance L_r /Resonant Capacitor C_r	1 μ H/22 nF
Power Switch S_m and S_a	STW20NM60FD
Output Diode D_o	BYV29X-600

By substituting the system and component specifications shown in Table 2 into Equations (38) and (39), the input-to-output transfer function $G_{vg}(s)$ can be found as

$$G_{vg}(s) = \frac{1.05 \times 10^6}{s^2 + 561.92s + 816.33 \times 10^3} \tag{41}$$

Furthermore, the duty-to-output transfer function is

$$G_{vd}(s) = \frac{-4.085 \times 10^3s + 208.1 \times 10^6}{s^2 + 561.92s + 816.33 \times 10^3} \tag{42}$$

After finding the transfer function of the proposed structure with resonant small signals by the dual time scale averaging method, the corresponding transfer function is compared with the small-signal transfer function of the traditional boost converter, which can be expressed as

$$\tilde{G}_{vd}(s) = \frac{-4.085 \times 10^3s + 215 \times 10^6}{s^2 + 151s + 843 \times 10^3} \tag{43}$$

From (42) and (43), the difference in zero value between them is not significant. However, the pole values in (42) are $-280.96 \pm j858.72$, and the pole values in (43) are $-75.5 \pm j915.04$. From these pole values of both equations, we can see that the proposed structure has a larger bandwidth because the resonance parameters are taken into considerations. That is to say, if the resonance parameters are ignored in the controller design, the designed controller is not suitable for the proposed structure.

4. Controller Design in Z-Domain

As shown in Figure 5, the design of the digital controller proposed in this paper is designed directly in the z – domain by the pole-zero configuration and the pole-zero cancellation design method. Figure 5 shows the digital control loop with loop gain $L(z)$:

$$L(z) = K \cdot C(z) \cdot G_{vd}(z) \cdot H(z) \cdot z^{-1} \tag{44}$$

where $G_{vd}(z)$ is the discrete transfer function of the boost converter, $H(z)$ is the divider gain, K is the PWM gain, AD gain, z^{-1} is the delay factor, and Equation (45) is the discrete transfer function of this controller, where z_{p1} and z_{p2} are poles, z_{o1} and z_{o2} are zeroes, and K_{c2} is the gain.

$$C(z) = K_{c2} \frac{(z - z_{o1})(z - z_{o2})}{(z - z_{p1})(z - z_{p2})} \tag{45}$$

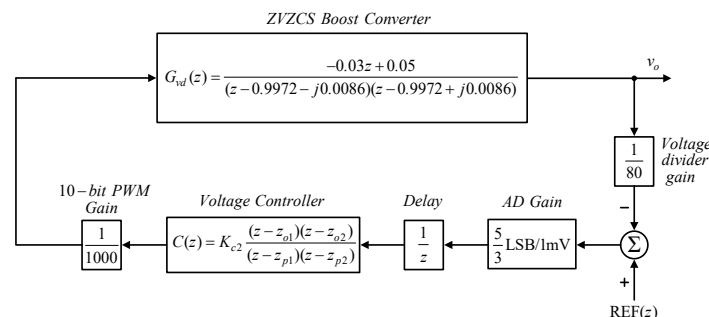


Figure 5. z-domain digital control loop.

When the controller is not added, the phase margin of the system known from the Bode plot of the loop gain is 14.7° . After designing the controller to make the system meet the prescribed specifications, the following steps will briefly describe the controller design.

Step 1: The gain margin is greater than 6 dB above and the crossover frequency is equal to one-tenth of the switching frequency.

Step 2: Configure poles z_{p1} and z_{p2} to match the gain margin and crossover frequency set by the system. Assuming a gain of $K_{c2} = 1$ and using the Matlab software assistant tool, named SISO, to configure and observe the two poles z_{p1} and z_{p2} several times, $z_{p1} = 0.178$ and $z_{p2} = 0.7$ are finally selected to meet the prescribed gain margin and switching frequency.

Step 3: After step 2, the crossover frequency is fixed and the system phase margin is adjusted. Finally, the phase margin is set to 60 degrees. The gained K_{c2} value, which is the value required to adjust the phase margin to 60 degrees, can be found by the Matlab syntax to obtain a gain K_{c2} value of 0.81.

$$[mag, phase, \omega] = bode(Lz) \quad (46)$$

$$K_{c2} = margin(mag, phase - 60, \omega)$$

After the above steps, the discrete transfer function of the controller can be obtained as follows along with $z_{o1} = 0.9972 + j0086$ and $z_{p2} = 0.9972 - j0086$:

$$C(z) = 0.81 \frac{(z - 0.9972 - j0.0086)(z - 0.9972 + j0.0086)}{(z - 0.178)(z - 0.7)} \quad (47)$$

The discrete transfer function of the above equation is converted into a difference equation, so that the difference equation can be written into programming language for digital control of the system.

$$\begin{aligned} u(n) &= a_2u(n-2) + a_1u(n-1) + b_2e(n-2) + b_1e(n-1) + b_0e(n) \\ &= -0.12u(n-2) + 0.87u(n-1) + 0.8e(n-2) - 1.6e(n-1) + 0.8e(n) \end{aligned} \quad (48)$$

Figure 6 shows the Bode plot of the system loop gain to verify the correctness of the designed controller.

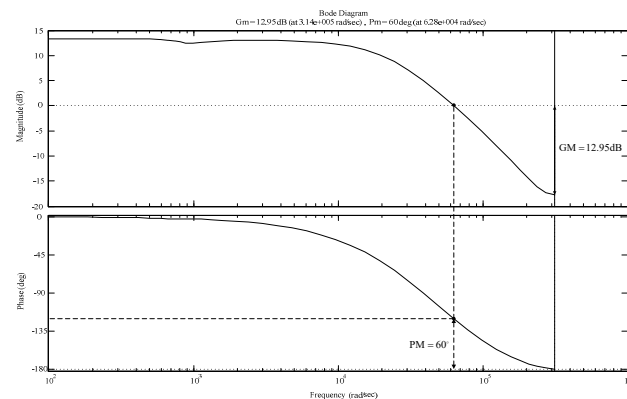


Figure 6. Bode plot of the system loop gain.

5. Auto-Adjustment Technique

In this paper, the auto-adjustment technique is implemented by using the lookup table to regulate the on-time and triggering instant of the auxiliary power switch to further improve the efficiency, especially at light loads, and to make the overall efficiency of the converter present a flat curve. In addition, when the load increases or decreases, since the efficiency does not vary regularly with the on-time of the preceding and following transients of the auxiliary power switch and the triggering instant relative to the main power switch, a look-up table is used instead of a complex calculation to determine the required on-time and triggering instant of the auxiliary power switch.

Figure 7a,b show the auto-adjustment technique for the auxiliary power switch operating at light load and rated load, respectively. This auto-adjustment technique is based on the following two conditions: first, the auxiliary power switch must reach zero current

cutoff, as shown in Figure 7 at points A and B; second, when the auxiliary power switch current i_{Sa} resonates to equal to the input current I_{Lm} , the main power switch is turned on, as shown in Figure 7 at points C and D. Therefore, by using the above-mentioned technique and using the input inductance current as the self-variable of the lookup table, the design steps are as follows.

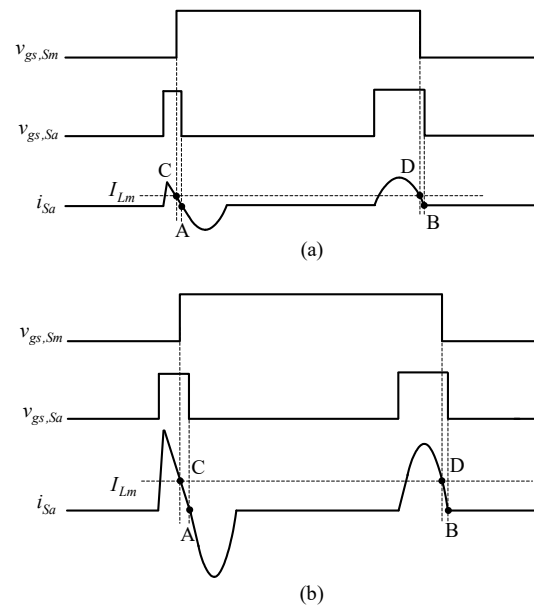


Figure 7. Auto-adjustment of turn-on time and triggering time of the auxiliary switch at (a) light load; (b) rated load.

Step 1: The light load to full load currents are divided into ten intervals and recorded separately based on no ADC sampling [20]. The sampled count value of the input inductance current is recorded.

Step 2: Within the set ten current intervals, the on-time before and after transients of the auxiliary power switch and the triggering instant relative to the main power switch are adjusted and recorded, respectively, from full load to light load.

Step 3: According to the above two steps, the turn-on time and triggering time of the auxiliary power switch can be determined by this prescribed look-up table.

It is worth mentioning that the addition of a hysteresis band is required to avoid the oscillation caused by the current interval change.

6. Design of Resonant Inductor and Resonant Capacitor

In this section, the resonant capacitor C_r and resonant inductor L_r are designed based on the results of states 1, 2 and 10 in Section 2. Without affecting the circuit operation behavior, it is determined that the overrun lead time of the auxiliary power switch must be less than or equal to one-tenth of the on time of the main power switch, i.e., less than or equal to 220 ns. Accordingly, the elapsed time $T_1 + T_2$ shown in Figure 2 must be less than or equal to 220 ns, where the elapsed time T_1 is the time it takes for the current i_{Sa} of the auxiliary power switch S_a to rise to the input inductance current I_{Lm} after the auxiliary power switch is turned on, and the elapsed time T_2 is the time it takes for the parasitic capacitor C_{Sm} of the main power switch to discharge to zero. The rise time t_r and the fall time t_f in the power switch instruction manual correspond to the characteristics of the current flowing through the power switch, so we can know that the time $T_2 \cong 20$ ns. Therefore, the elapsed time T_1 is less than or equal to 200 ns [21], so the following equation can be found:

$$T_1 = \frac{C_r(V_{Cr1} - V_{Cr10})}{(I_{Lm} - I_o)} \leq 200 \text{ ns} \quad (49)$$

where V_{Cr1} can be obtained by state 2 as follows:

$$V_{Cr1} = V_o - \frac{L_r I_{Lm}}{T_2} \quad (50)$$

where I_{Lm} is the average value of the rating input inductance current, and V_{Cr10} can be obtained by state 10 as follows:

$$V_{Cr10} = \frac{I_{Lm} T_{10}}{C_r + C_{Sm}} \left(1 + \frac{C_{Sm}}{C_r}\right) + \frac{L_r I_{Lm}}{T_{10}} \quad (51)$$

where the elapsed time T_{10} can be known from the following equation:

$$\begin{aligned} \Delta Q &= C_r V_o = 0.5 I_{Lm} T_{10} \\ &= 550\text{p} \cdot 200 = 0.5(2.56) T_{10} \end{aligned} \quad (52)$$

Therefore, T_{10} can be found as 86 ns.

Sequentially, let the resonant frequency f_2 be greater than or equal to ten times the switching frequency, i.e., $\omega_2 \geq 2\pi \cdot 10^6 \text{ rad/sec}$, and substitute (47) and (48) into (49) to obtain

$$\begin{aligned} C_r \left[V_o - \frac{L_r I_{Lm}}{T_2} - \frac{I_{Lm} T_2}{C_r + C_{Sm}} \left(1 + \frac{C_{Sm}}{C_r}\right) + \frac{L_r I_{Lm}}{T_2} \right] &\leq 200 \text{ ns} \\ \Rightarrow \frac{C_r \left[200 - \frac{\frac{1}{4\pi^2 \omega_2^2} (2.56)}{20\text{ns}} - \frac{(2.56)(85\text{ns})}{C_r + 550\text{p}} \left(1 + \frac{550\text{p}}{C_r}\right) + \frac{\frac{1}{4\pi^2 f_2^2} (2.56)}{85\text{ns}} \right]}{(2.56-2)} &\leq 200 \text{ ns} \end{aligned} \quad (53)$$

The resonant capacitance C_r can be obtained as 21.45 nF from (53). The allowable error of the actual capacitance is considered, so the resonant capacitance C_r is chosen as 22 nF. After obtaining the resonant capacitance C_r , the resonant inductance L_r can be obtained as

$$L_r \leq \frac{1}{4\pi^2 f_2^2 C_r} = \frac{1}{4\pi^2 (10^6)^2 22 \text{ n}} \quad (54)$$

Therefore, the value of resonance inductance can be obtained as $L_r \leq 1.15 \mu\text{H}$, so this paper selects the resonance inductance as 1 μH .

7. Simulated and Experimental Results

The system specifications are shown in Table 2 in Section 3. In this section, the proposed converter and control strategy will be verified by using Active-HDL combined with Matlab/Simulink as the simulation environment, and, finally, the effectiveness will be verified by using a real circuit. In this paper, the simulated controller parameters are simulated by the controller parameters designed in (50). The controller parameters are fine-tuned to $a_2 = -0.12$, $a_1 = 0.88$, $b_2 = 1.2$, $b_1 = 1$ and $b_0 = 1$. However, the parasitic components of the line must be considered in the implementation of this circuit. Consequently, the controller parameters are fine-tuned to $a_2 = -0.14$, $a_1 = 0.88$, $b_2 = 1$, $b_1 = 0.88$ and $b_0 = 1$.

7.1. Simulated Waveforms

The purpose of the software simulation is used to demonstrate the feasibility of the proposed converter. Figure 8 shows the system simulation block diagram, which includes the proposed structure, the digital control block generated by the Active-HDL software, the sampling circuit module, the peripheral auxiliary power supply, and the oscilloscope. Furthermore, the simulation environment is based on the 2021a MATLAB and Simulink software with the system specifications shown in Table 2. In addition, the power switches used herein are non-ideal, but the passive components are all ideal. Furthermore, the circuit is simulated at rated load. The value of C_{Sm} based on [21] is set at 550 pF, which is called equivalent capacitance affected by the value of v_{CSm} .

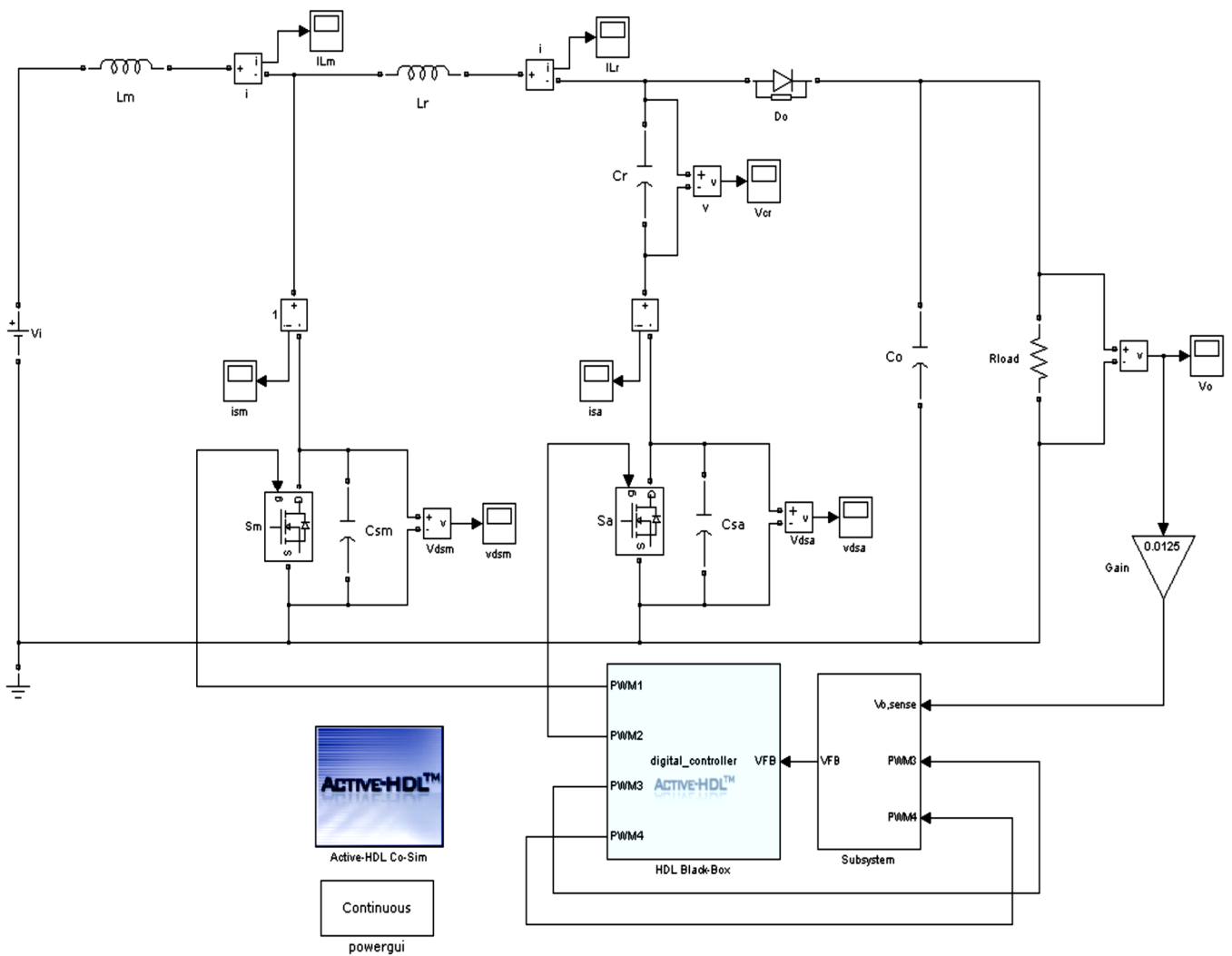


Figure 8. System simulation block diagram.

Figure 9 shows the gate driving signal v_{gs,S_m} for the main power switch S_m and the gate driving signal v_{gs,S_a} for the auxiliary power switch S_a , where the gate driving signal v_{gs,S_a} possesses the pre- and post-duty cycle of the gate driving signal v_{gs,S_m} .

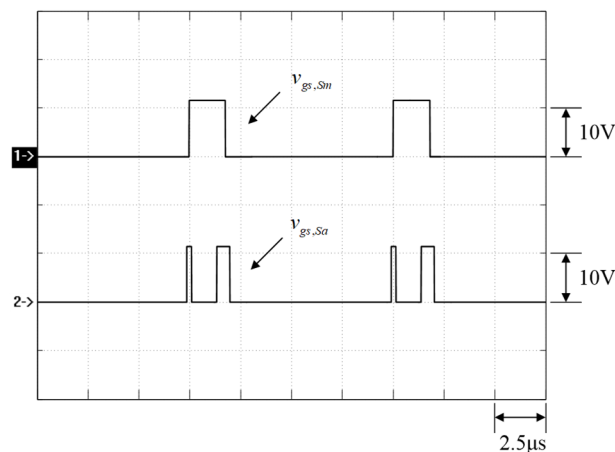


Figure 9. Simulated gate driving signals for main power switch S_m and auxiliary power switch S_a .

Figure 10 shows the waveforms of the main power switch, where v_{gs,S_m} is the gate driving signal, v_{ds,S_m} is the voltage across S_m , i_{S_m} is the current in the switch S_m . Figures 11 and 12 are zoomed-in waveforms of Figure 10.

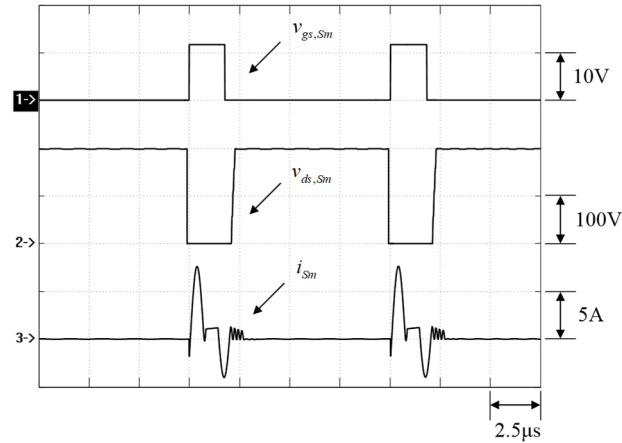


Figure 10. Simulated waveforms related to the main power switch S_m .

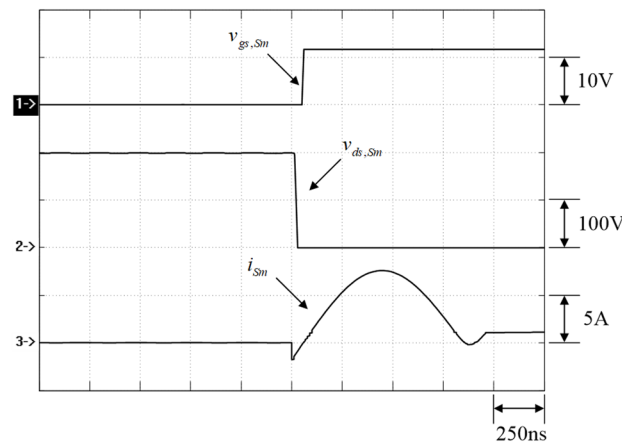


Figure 11. Simulated zoomed-in transient waveforms before main power switch S_m .

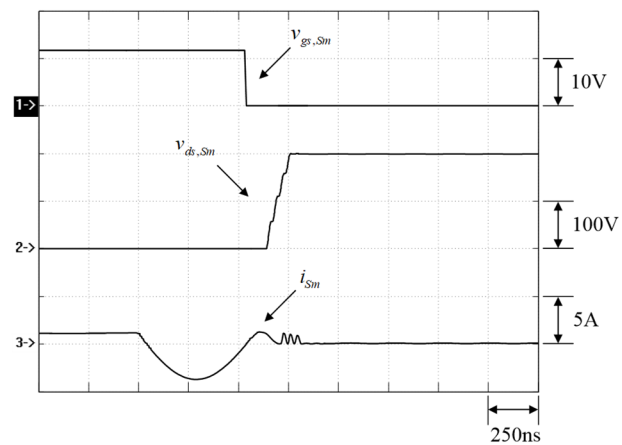


Figure 12. Simulated zoomed-in transient waveforms after the main power switch S_m .

Figure 13 shows the waveforms of the auxiliary power switch S_a , where v_{gs,S_a} is the gate driving signal, v_{ds,S_a} is the voltage on S_a and i_{S_a} is the current in S_a . Figures 14 and 15 are zoomed-in waveforms of Figure 13.

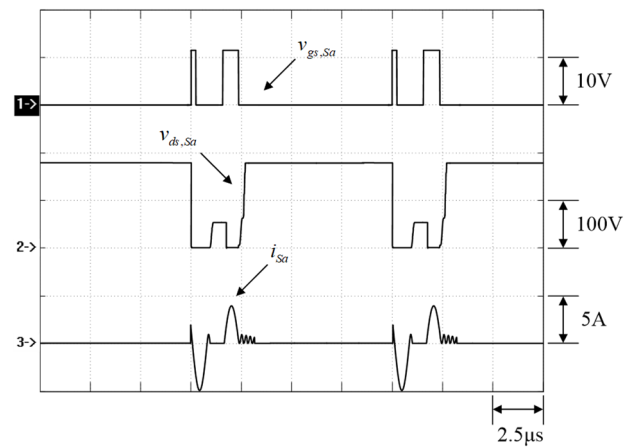


Figure 13. Simulated waveforms related to the auxiliary power switch S_a .

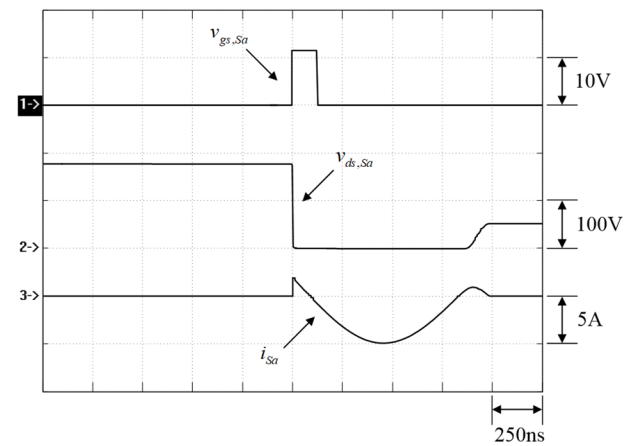


Figure 14. Simulated zoomed-in transient waveforms before the auxiliary power switch S_a .

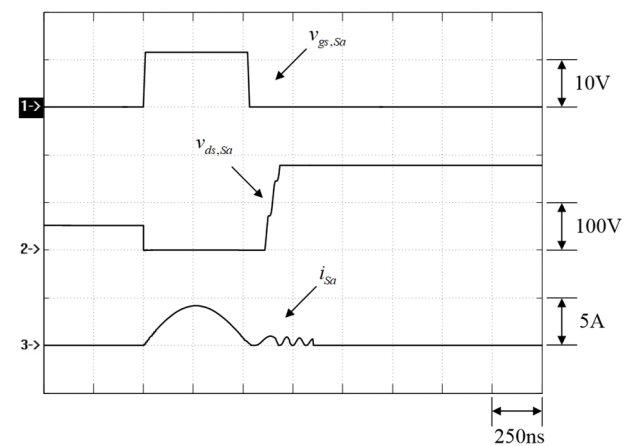


Figure 15. Simulated zoomed-in transient waveforms after the auxiliary power switch S_a .

Figure 16 shows the associated waveforms of the resonant elements, where i_{Lr} is the current in the resonant inductor L_r and v_{Cr} is the voltage across the resonant capacitor C_r .

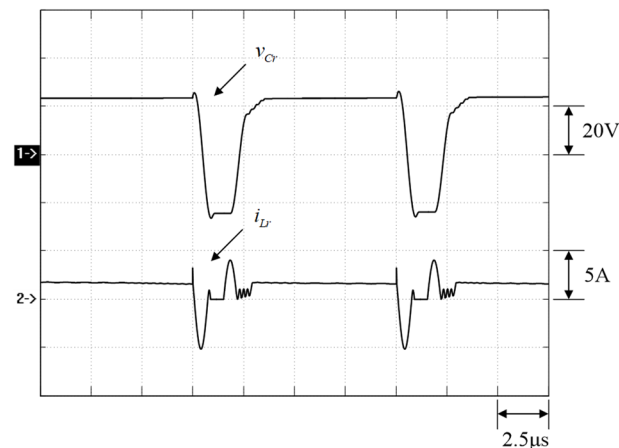


Figure 16. Simulated resonant waveforms.

From the above simulated results, it can be seen that when the auxiliary power switch S_a is turned on before the main power switch S_m , the auxiliary power switch current i_{S_a} rises rapidly to a level greater than the input inductance current I_{L_m} . According to Kirchhoff's current law, the parasitic capacitor C_{S_m} of the main power switch starts to discharge the resonant circuit until it discharges to zero, then the body diode of the main power switch D_{S_m} turns on, and the voltage v_{ds,S_m} of the main power switch is clamped to zero, and after this, the main power switch S_m is turned on with ZVT, as shown in Figures 10 and 11.

The current waveforms in Figures 10, 12, 13, 15 and 16 show that when the auxiliary power switch S_a is cut off, the parasitic capacitance C_{S_a} of the auxiliary power switch, the resonant inductor L_r , the resonant capacitor C_r and the parasitic capacitor C_{S_m} of the main power switch form a resonance loop, resulting in a ringing phenomenon, so the corresponding currents will ring.

From Figures 11, 14 and 16, it can be seen that when the auxiliary power switch current i_{S_a} resonates to zero, the parasitic capacitor C_{S_a} , resonant inductor L_r and resonant capacitor C_r form a resonance loop, so a small resonant current is generated, and the corresponding small voltage across C_r will ring.

As can be seen from Figure 12, when the main power switch S_m is turned off, the ringing phenomenon on the main power switch current i_{S_m} causes the voltage v_{ds,S_m} across the main power switch S_m to be charged slowly, so the voltage $v_{C_{S_m}}$ rises slowly and the resulting overshoot current becomes small. In addition, the auxiliary power switch S_a is turned on after the main power switch S_m . When the auxiliary power switch current i_{S_a} resonates to the input inductance current I_{L_m} , according to Kirchhoff's current law, the main power switch S_m is turned off at this time, so that the main power switch S_m is turned off with ZCT.

As can be seen from Figures 13 and 15, when the auxiliary power switch current i_{S_a} drops to zero, the auxiliary power switch S_a is turned off with ZCS.

7.2. Experimental Waveforms

The purpose of the experimental measurement is used to verify the effectiveness of the proposed converter. In addition, the circuit is experimented at rated load.

Figure 17 shows the waveforms of the gate driving signal v_{gs,S_m} of the main power switch S_m and the gate driving signal v_{gs,S_a} of the auxiliary power switch S_a at rated load, where the gate driving signal v_{gs,S_a} possesses the pre- and post-duty cycle of the gate driving signal v_{gs,S_m} .

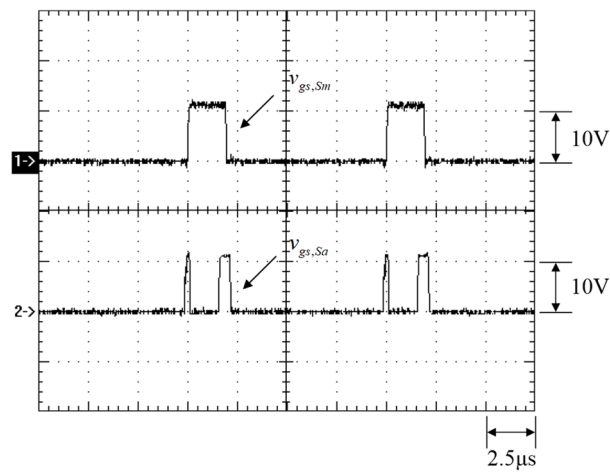


Figure 17. Measured gate driving signals of the main power switch S_m and auxiliary power switch S_a .

Figure 18 shows the waveforms of the main power switch S_m at rated load, where v_{gs,S_m} is the gate driving signal, v_{ds,S_m} is the voltage on S_m and i_{S_m} is the current in S_m . Figures 19 and 20 are the zoomed-in versions of Figure 18.

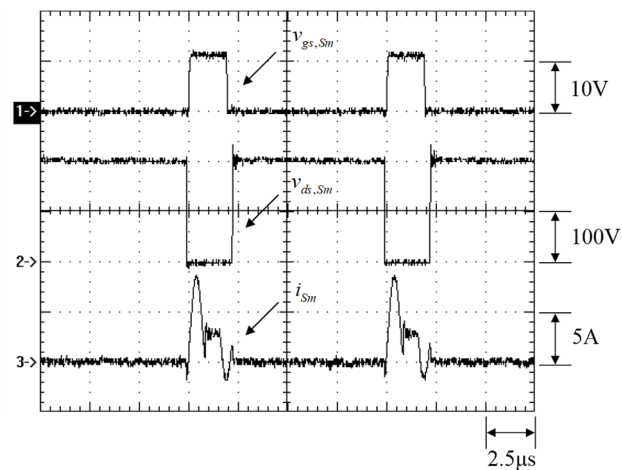


Figure 18. Measured waveforms related to the main power switch S_m .

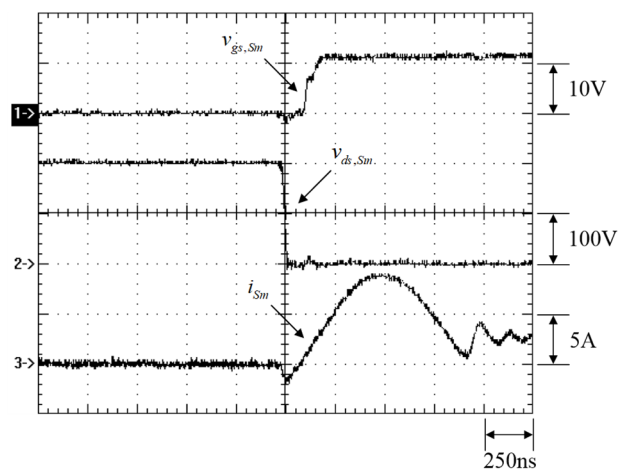


Figure 19. Measured zoomed-in transient waveforms before the auxiliary power switch S_m .

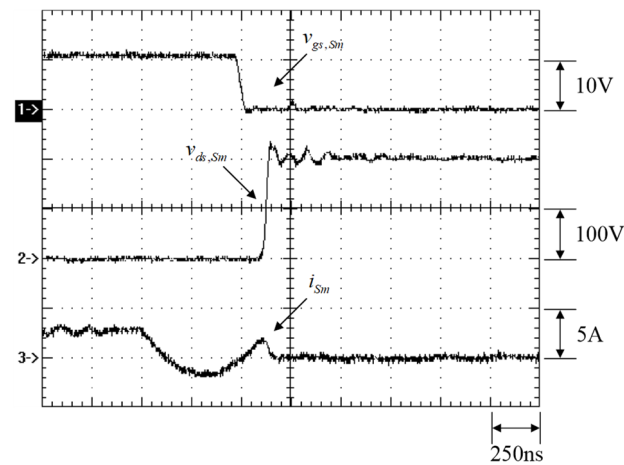


Figure 20. Measured zoomed-in transient waveforms before the auxiliary power switch S_m .

Figure 21 shows the waveforms of the auxiliary power switch S_a at rated load, where v_{gs,S_a} is the gate driving signal, v_{ds,S_a} is the voltage on S_a and i_{S_a} is the current in S_a . Figures 22 and 23 are the zoomed-in versions of Figure 21.

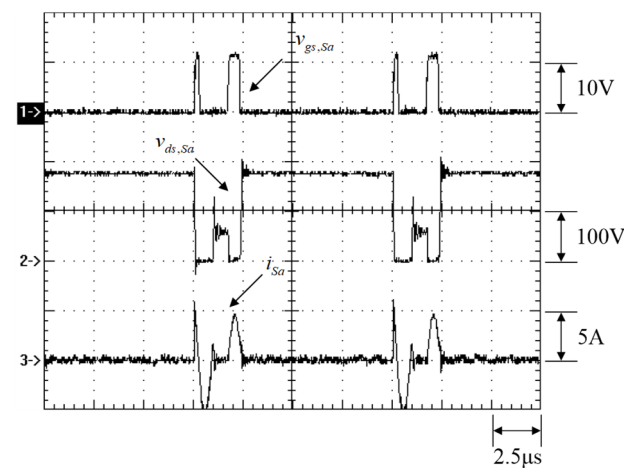


Figure 21. Measured waveforms related to the main power switch S_a .

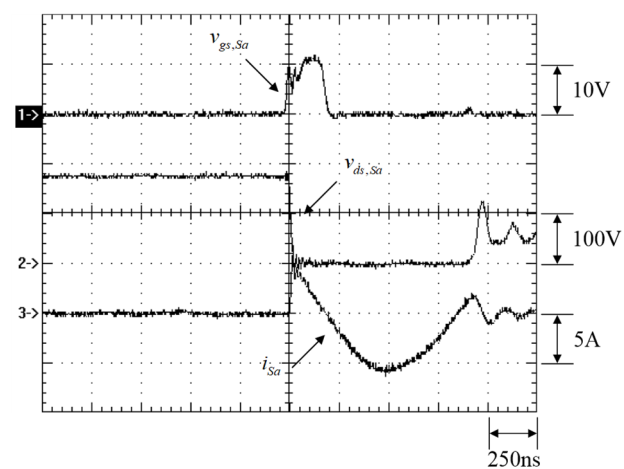


Figure 22. Measured zoomed-in transient waveforms before the auxiliary power switch S_a .

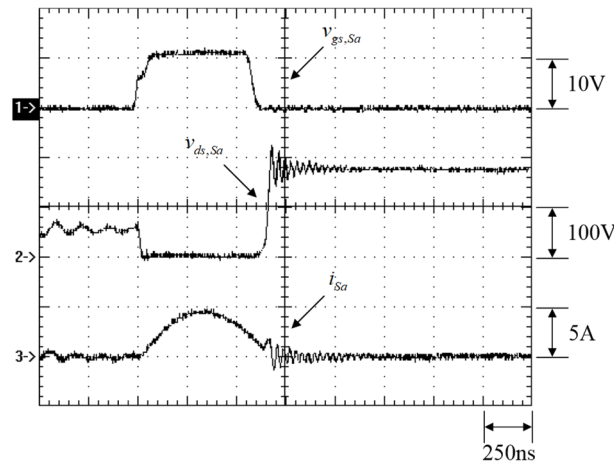


Figure 23. Measured zoomed-in transient waveforms after the auxiliary power switch S_a .

Figure 24 shows the waveforms of the resonant element under the rated load, where i_{Lr} is the current in the resonant inductor L_r and v_{Cr} is the voltage on the resonant capacitor C_r .

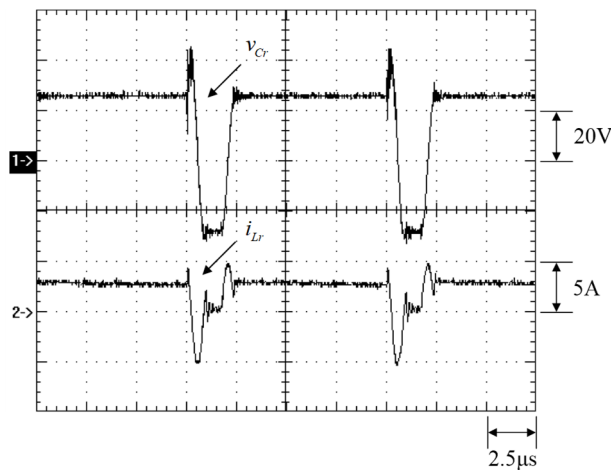


Figure 24. Measured resonant waveforms.

Figure 25 shows the efficiencies of the proposed structure under different output powers with soft switching and auto-adjustment technique, the proposed structure with soft switching and no auto-adjustment technique, and the traditional structure with hard switching.

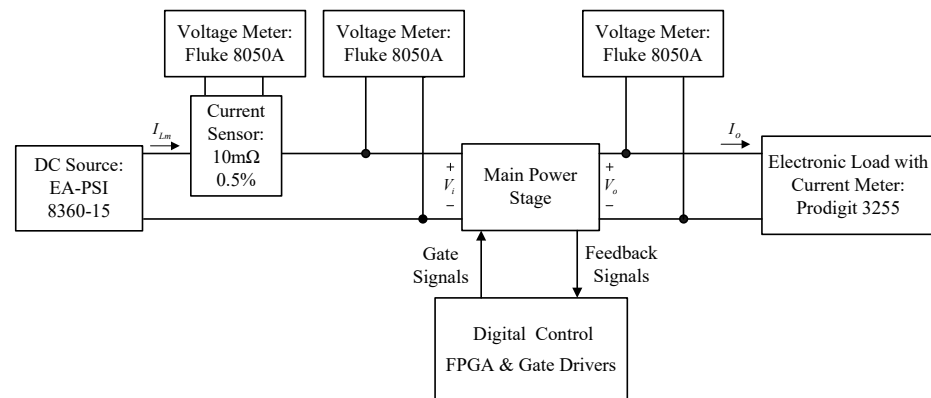


Figure 25. Efficiency measurement block diagram.

7.3. Efficiency Measurement

As shown in Figure 25, a current-sensing resistor is connected in series with the input current path, and a digital meter (Fluke 8050A, manufactured by FLUKE Co., Everett, Washington, USA) is used to measure the voltage across this resistor to obtain the input current value and the input voltage using a digital meter to obtain the input power. On the output side, an electronic load (Prodigit 3255, manufactured by PRODIGIT Co., Taipei, Taiwan) is used to provide the load current required by the converter, and the output voltage is measured using a digital meter to obtain the output power. Finally, the input power and output power are used to calculate the efficiency of the actual circuit operation. In Figure 26, curves of efficiency versus output power under soft switching with and without auto-adjustment and hard switching are displayed.

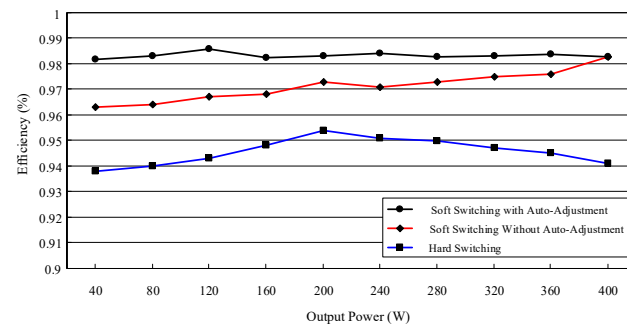


Figure 26. Curves of efficiency versus output power under soft switching with and without auto-adjustment, and hard switching.

7.4. Experimental Setup

As shown in Figure 27, the photo of the experimental setup is displayed.

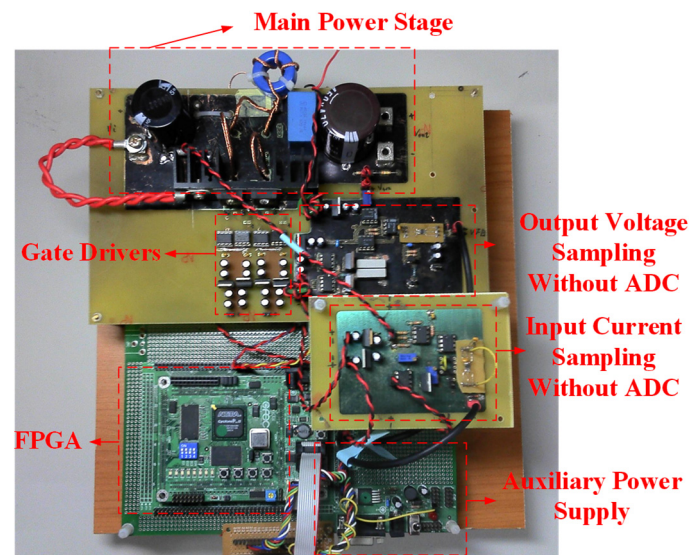


Figure 27. Photo of the experimental setup.

From the above experimental results, when the auxiliary power switch S_a precedes the main power switch S_m , the auxiliary power switch current i_{sa} rises rapidly to greater than the input inductance current I_{Lm} ; according to Kirchhoff's current law, the parasitic capacitor C_{Sm} of the main power switch starts to discharge the resonant circuit until the discharge reaches zero. Therefore, the body diode D_{Sm} of the main power switch turns on and the voltage $v_{ds,Sm}$ of the main power switch is clamped to zero, so the main power switch S_m is turned on with ZVT, as shown in Figures 17 and 19.

The current waveforms in Figures 19, 22 and 24 show that the resonant inductor current i_{Lr} flows in the opposite direction when operating in mode 6, and when the resonant inductor current i_{Lr} resonates to zero, the body diode D_{Sa} of the auxiliary power switch turns from on to off, generating the reverse recovery current, and this current flows through the parasitic capacitor C_{Sa} of the auxiliary power switch, the resonant inductor L_r , the resonant capacitor C_r , the parasitic capacitor C_{Sm} of the main power switch and the parasitic inductor of the line, causing the ringing phenomenon. Since all belong to the same resonant tank, so this resonance will be reflected in the currents as well as also being reflected in the voltage $v_{ds,Sa}$ of the auxiliary power switch.

As can be seen from Figure 20, there is a delay in the voltage $v_{ds,Sm}$ across the main power switch. The reason for this can be seen from state 9, when the main power switch S_m is turned off from on, because the power switch will delay the cut-off, so the main power switch current i_{Sm} continues to resonate up, and when it rises to the input current, the voltage $v_{ds,Sm}$ across the main power switch is larger than the output voltage, the resonant inductor L_r begins to be magnetized. According to the Kirchhoff's current law, the main power switch current i_{Sm} begins to fall to zero, so the main power switch S_m has ZCT turn-off.

From Figure 23, it can be seen that when the auxiliary power switch S_a is turned off, the voltage $v_{ds,Sa}$ across the auxiliary power switch and the current i_{Sa} have the ringing phenomenon. The reason is that the output diode D_o is delayed when changing from state 10 to state 11. Therefore, the resonant inductor current i_{Lr} will flow through the parasitic capacitor C_{Sa} of the auxiliary power switch, forming a resonant circuit and hence causing the auxiliary power switch to have ZCS turn-off.

From Figure 23, it can be seen that when the auxiliary power switch S_a is turned on, the rapid rise of the auxiliary power switch current i_{Sa} and the effect of the parasitic inductance of the line cause noise to be generated across the resonant capacitor C_r , but this noise does not affect the circuit operation behavior. In addition, from Figure 23, the voltage v_{Cr} across the resonant capacitor C_r also has a ringing at the negative voltage due to the ringing on the resonant inductor current i_{Lr} .

From Figure 26, it can be seen that under the input voltage of 156 V and the output voltage of 200 V as shown in Table 2, the proposed structure with/without auto-adjustment can effectively improve the overall efficiency of the converter in the output power range (40 W ~ 400 W). The difference in efficiency between soft switching with auto-adjustment and hard switching is 4.8%, whereas the difference in efficiency between soft switching with auto-adjustment and soft switching without auto-adjustment is about 2.1%. Most importantly, the proposed structure with the addition of the auto-adjustment technique not only further improves the efficiency, but also makes the efficiency show an approximately horizontal curve.

8. Conclusions

From the experimental results, it can be seen that the main power switch has both ZVT and ZCT, and the auxiliary power switch also has ZCS. In addition, the lookup table is also added to realize the auto-adjustment technique to regulate the on-time and triggering position of the auxiliary power switch to further improve the efficiency, especially at light load, thus making the overall efficiency of the converter present a flat curve. From the experimental measurements, the maximum efficiency of the proposed converter is 98.5% and the light load efficiency is 98.1%, and the overall system efficiency is above 98%. Regarding the system control, the direct design of the digital controller under z-domain can effectively stabilize the output voltage of the converter and achieve the purpose of fully digitalized control.

Author Contributions: Conceptualization, K.-I.H., Z.-F.L. and P.-C.T.; methodology, K.-I.H. and P.-C.T.; software, Z.-F.L.; validation, Z.-F.L.; formal analysis, Z.-F.L.; investigation, Z.-F.L.; resources, K.-I.H.; data curation, P.-C.T.; writing—original draft preparation, K.-I.H.; writing—review and editing, K.-I.H.; visualization, Z.-F.L.; supervision, K.-I.H.; project administration, K.-I.H.; funding acquisition, K.-I.H. All authors have read and agreed to the published version of the manuscript.

Funding: This research was funded by the Ministry of Science and Technique, Taiwan, under the Grant Number: MOST 110-2221-E-027-045-MY2.

Data Availability Statement: No new data were created or analyzed in this study. Data sharing is not applicable to this article.

Conflicts of Interest: The authors declare no conflict of interest.

References

1. Tabisz, W.A.; Jovanic, M.M.; Lee, F.C. High-frequency multi-resonant converter technique and its applications. In Proceedings of the 1990 Fourth International Conference on Power Electronics and Variable-Speed Drives, London, UK, 17–19 July 1990; pp. 1–8.
2. Jabbari, M.; Farzanehfar, H. New resonant step-down/up converters. *IEEE Trans. Power Electron.* **2010**, *25*, 249–256. [[CrossRef](#)]
3. Wang, C.-M. New family of zero-current-switching PWM converters using a new zero-current-switching PWM auxiliary circuit. *IEEE Trans. Ind. Electron.* **2006**, *53*, 768–777. [[CrossRef](#)]
4. Shuai, P.; De Novaes, Y.R.; Canales, F.; Barbi, I. A non-insulated resonant boost converter. In Proceedings of the 2010 Twenty-Fifth Annual IEEE Applied Power Electronics Conference and Exposition (APEC), Palm Springs, CA, USA, 21–25 February 2010; pp. 550–556.
5. Huang, W.; Gao, X.; Bassan, S.; Moschopoulos, G. Novel dual auxiliary circuits for ZVT-PWM converters. *Can. J. Electr. Comput. Eng.* **2008**, *33*, 153–160. [[CrossRef](#)]
6. Adib, E.; Farzanehfar, H. Zero-voltage-transition PWM converters with synchronous rectifier. *IEEE Trans. Power Electron.* **2010**, *25*, 105–110. [[CrossRef](#)]
7. Yang, S.-P.; Lin, J.-L.; Chen, S.-J. A novel ZCZVT forward converter with synchronous rectification. *IEEE Trans. Power Electron.* **2006**, *21*, 912–922. [[CrossRef](#)]
8. Bodur, H.; Bakan, A.F. A new ZVT-ZCT-PWM DC-DC converter. *IEEE Trans. Power Electron.* **2010**, *19*, 676–684. [[CrossRef](#)]
9. Hwu, K.-I.; Shieh, J.-J.; Jiang, W.-Z. Interleaved boost converter with ZVT-ZCT for main switches and ZCS for auxiliary switch. *Appl. Sci.* **2020**, *10*, 2033. [[CrossRef](#)]
10. Yau, Y.-T.; Hwu, K.-I.; Jiang, W.-Z. Two-phase interleaved boost converter with ZVT turn-on for main switches and ZCS turn-off for auxiliary switches based on one resonant loop. *Appl. Sci.* **2020**, *10*, 3881. [[CrossRef](#)]
11. Yau, Y.-T.; Hwu, K.-I.; Shieh, J.-J. Simple structure of soft switching for boost converter. *Energies* **2020**, *13*, 5448. [[CrossRef](#)]
12. Akin, B. An Improved ZVT-ZCT PWM DC-DC boost converter with increased efficiency. *IEEE Trans. Power Electron.* **2014**, *29*, 1919–1926. [[CrossRef](#)]
13. Altıntaş, N.; Bakan, A.F.; Aksoy, I. A novel ZVT-ZCT-PWM boost converter. *IEEE Trans. Power Electron.* **2014**, *29*, 256–265. [[CrossRef](#)]
14. Yi, J.H.; Choi, W.; Cho, B.H. Zero-voltage-transition interleaved boost converter with an auxiliary coupled inductor. *IEEE Trans. Power Electron.* **2017**, *32*, 5917–5930. [[CrossRef](#)]
15. Khorasani, R.R.; Adib, E.; Farzanehfar, H. ZVT resonant core reset forward converter with a simple auxiliary circuit. *IEEE Trans. Ind. Electron.* **2018**, *65*, 242–250. [[CrossRef](#)]
16. Xia, Y.; Ayyanar, R. Naturally adaptive, low-loss zero-voltage-transition circuit for high-frequency full-bridge inverters with hybrid PWM. *IEEE Trans. Power Electron.* **2018**, *33*, 4916–4933. [[CrossRef](#)]
17. Zhang, X.; Qian, W.; Li, Z. Design and analysis of a novel ZVZCT boost converter with coupling effect. *IEEE Trans. Power Electron.* **2017**, *32*, 8992–9000. [[CrossRef](#)]
18. Rezvanyvardom, M.; Mirzaei, A. Zero-voltage transition nonisolated bidirectional buck-boost DC-DC converter with coupled inductors. *IEEE J. Emerg. Sel. Top. Power Electron.* **2021**, *9*, 3266–3275. [[CrossRef](#)]
19. Sun, J.; Grotstollen, H. Averaged modelling of switching power converters: Reformulation and theoretical basis. In Proceedings of the 23rd Annual IEEE Power Electronics Specialists Conference, Toledo, Spain, 29 June–3 July 1992; pp. 1165–1172.
20. Hwu, K.I.; Yau, Y.T. Applying an FPGA-counter-based control strategy to multiple SR outputs of a forward converter. In Proceedings of the 2006 37th IEEE Power Electronics Specialists Conference, Jeju, Republic of Korea, 18–22 June 2006; pp. 1–4.
21. Available online: <https://pdf1.alldatasheet.com/datasheet-pdf/view/158402/STMICROELECTRONICS/STB11NM60FD.html> (accessed on 12 April 2021).

Disclaimer/Publisher’s Note: The statements, opinions and data contained in all publications are solely those of the individual author(s) and contributor(s) and not of MDPI and/or the editor(s). MDPI and/or the editor(s) disclaim responsibility for any injury to people or property resulting from any ideas, methods, instructions or products referred to in the content.